

Chapter 4

Detecting photons from the CoRoT planets

This chapter focuses on the study of planet's secondary eclipses and the orbital phase variations. The amplitude of the secondary eclipse of a planet gives a measurement of the integrated flux of the planet's day-side hemisphere, relative to the integrated flux from the visible side of the stellar disk. The phase of the secondary eclipse gives a measurement of the eccentricity of the planet's orbit. The amplitude of the planet's orbital phase variation gives a measurement of the flux from the night-side hemisphere of the planet (minimum) relative to the planet's day-side (maximum). The shape of the phase variation gives an insight on the planet atmospheric circulation, if the dominant component of the planet flux is its thermal emission, or an insight on the microscopic properties on the reflective material at the surface of the planet, if the dominant flux is the reflected starlight.

The first detections of the secondary eclipses of an exoplanet were made by Charbonneau et al. (2005) and Deming et al. (2005), followed by the detections of planet's orbital phase variations published in Harrington et al. (2006) and Knutson et al. (2007a). These detections were made from space to increase the photometric precision, and in the infrared where the planet's flux is stronger. The first ground based detections of the thermal emission of an exoplanet was recently made by de Mooij & Snellen (2009) and Sing & López-Morales 2009, and since the secondary eclipse of several other exoplanets were observed (e.g. CoRoT-1b in Gillon et al. 2009, CoRoT-2b in Alonso et al. 2010). The first secondary eclipses in the visible from space were recently detected with CoRoT and Kepler for CoRoT-1b and 2b (Alonso et al. 2009b,a; this work) and HAT-P-7 (Borucki et al., 2009). The observation of secondary eclipses in multiple bandpass give information on the planet's atmospheric properties (e.g. planet temperature, nature of reflective particles).

For planets around active stars, the stellar variability hinders the detection of secondary eclipses and orbital phase variations. As mentioned in Chapter 2, the IRF recon-

structs all signals at the orbital period of the planet, and presented itself as a suitable tool to filter the CoRoT light curves and search for the planet photometric signature.

The theory behind the secondary eclipse of planets and their orbital phase variations is presented in Section 4.1. After describing in Section 4.2 the method followed to search and measure secondary eclipses, the technique is applied to CoRoT-1b and CoRoT-2b in Section 4.3. The achievements of this chapter are then discussed in Section 4.4 and conclusions are drawn in Section 4.5.

Some of the work presented in this chapter was carried out as part of the CoRoT collaboration and published in Alonso et al. (2009a,b). Specifically, the method described in this chapter was one of several methods used to detect the secondary eclipses of CoRoT-1b and 2b. The method was optimised further since this publication, leading to an improvement in the significance of the detections.

4.1 Theory of the secondary eclipse and orbital phase variations

This section summarises the equations and concepts on secondary eclipses used in the chapter. It explores the dependence of the secondary depth with R_p/R_* , a/R_* , the Bond albedo A_B , and the re-distribution parameter f . It derives expected depths for the secondary eclipse of the CoRoT planets published to date (or close to publication).

4.1.1 Planet's emission

The flux emitted by the planet is:

$$F_p = F_{\star, \text{ reflected by planet}} + F_{p, \text{ thermal emission}} + F_{p, \text{ internal}} \quad (4.1)$$

where $F_{p, \text{ thermal emission}}$ is the flux from the star absorbed and re-emitted by the planet, and $F_{p, \text{ internal}}$ the planet internal heat (e.g. due to contraction heating or tidal heating).

The Bond Albedo A_B of a planet is defined as the fraction of incident power that is reflected back by the planet, averaged over all the wavelengths and phase angles¹, therefore:

$$F_{\star, \text{ reflected by planet}} = A_B F_{\star, \text{ received by planet}} \quad (4.2)$$

$$F_{\star, \text{ absorbed by planet}} = (1 - A_B) F_{\star, \text{ received by planet}} \quad (4.3)$$

The star can be approximated as a black body, thus $F_{\star} = 4\pi R_{\star}^2 \sigma_{\text{SB}} T_{\star}^4$ (σ_{SB} is the Stefan-Boltzmann constant) and the stellar flux received by the planet can be expressed as:

$$F_{\star, \text{ received by planet}} = \pi R_p^2 \frac{F_{\star}}{4\pi a^2} = \frac{1}{4} \left(\frac{R_p}{a} \right)^2 F_{\star} \quad (4.4)$$

¹The phase angle is the angle between the incident flux and the line of sight

4.1.2 Secondary eclipse

Depth

The depth of the secondary eclipse is $\frac{\Delta F}{F} = \frac{F_p}{F_* + F_p}$. As $F_p \ll F_*$ (4 or more orders of magnitude smaller), the depth of the secondary eclipse can be approximated by:

$$\frac{\Delta F}{F} = \frac{F_p}{F_*} \quad (4.5)$$

In the case where the planet emission only comes from the stellar flux reflected by the planet ($F_p = F_{*, \text{reflected by planet}}$) – e.g. for a planet with no thermal emission and internal heat – from equations 4.4 and 4.2 the depth of the secondary eclipse can be expressed as:

$$\frac{F_p}{F_*} = \frac{A_B}{4} \left(\frac{R_p}{a} \right)^2 = \frac{A_B}{4} \left(\frac{R_p}{R_*} \right)^2 \left(\frac{R_*}{a} \right)^2 \quad (4.6)$$

In practice, the albedo measured from the depth of the planet's occultation is the geometric albedo A_g , which is the fraction of incident light reflected back at zero phase angle (i.e. the configuration at occultation). $A_g = \frac{2}{3}A_B$ for Lambertian isotropic reflectance (i.e. constant for all angles of incidence) (Rowe et al., 2006). The calculations in this chapter are made under the assumption that $A_B = A_g$. The analysis will be repeated in the near future for $A_g = \frac{2}{3}A_B$.

Phase

The phase of a planet secondary eclipse ϕ_{sec} with regards to the phase of the transit (set to 0) can be computed by solving Kepler's equation numerically, for the range of possible e and ω determined by radial velocity measurements. To the first order in e (for $e \leq 0.2$), Winn (2010) give an analytic formula to derive the phase of the secondary eclipse (the transit is at phase 0):

$$\phi_{sec} \approx \frac{P}{2} \left[1 + \frac{2e \cos \omega}{\pi} \right] \quad (4.7)$$

where, P is the planet orbital period, e is the eccentricity and ω the angle to the periastron. The phase of the secondary eclipse provides a measurement of $e \cos \omega$, and the radial velocity curve a measurement of $e \sin \omega$ (Winn, 2010). When the information derived from both is combined together, e and ω can be derived individually.

4.1.3 Planet's equilibrium temperature

If we approximate the planet as a black body, the thermal emission of the planet is $F_{p, \text{thermal emission}} = F_{p, \text{black body}} = 4\pi R_p^2 \sigma_{SB} T_p^4$.

To account for the efficiency of the energy transport from the planet surface receiving the stellar flux to the planet surface re-emitting this flux, a redistribution factor f is introduced such that:

$$F_{p, \text{ thermal emission}} = \frac{1}{4f} F_{p, \text{ black body}} \quad (4.8)$$

where $\frac{1}{4f}$ represents the fraction of the total planet surface ($4\pi R_p^2$) that is reemitting the absorbed stellar flux. If the energy transport from the day to the night side of the planet is efficient, then the whole planet is reemitting (isothermal reemission over the whole sphere) and $\frac{1}{4f} = 1$, i.e. $f = 1/4$. If the energy transport is inefficient and only the day-side of the planet (half sphere) is reemitting, then $\frac{1}{4f} = 0.5$ and $f = 1/2$. If the energy transport is even less efficient and only a portion on the day-side is reemitting, then $\frac{1}{4f} < 0.5$ and $f > 1/2$.

If the planet is in thermal equilibrium,

$$F_{p, \text{ thermal emission}} = F_{\star, \text{ absorbed by planet}} \quad (4.9)$$

From the planet black body approximation and equations 4.8, 4.9, 4.3 and 4.4, the planet equilibrium temperature can be derived as:

$$T_{p, eq} = [f (1 - A_B)]^{1/4} \sqrt{\frac{R_{\star}}{a}} T_{\star} \quad (4.10)$$

From the black body emissions of the planet and the star, using equations 4.5 and 4.10, and assuming that the planet is in thermal equilibrium and that the planet thermal emission dominates over the other components of the planet flux, the expected depth of the planet secondary eclipse can be expressed as:

$$\frac{\Delta F}{F} = f (1 - A_B) \left(\frac{R_{\star}}{a}\right)^2 \left(\frac{R_p}{R_{\star}}\right)^2 \quad (4.11)$$

Several effects can take the planet out of thermal equilibrium, in which case equation 4.11 will not reflect the true depth of the secondary eclipse. The secondary eclipse can appear deeper than calculated with equation 4.11, if the planet radiates more than the energy than it receives from its star – for instance if the planet has an internal heat due to the contraction of the planet if the planet is young, or to tidal heating. The secondary eclipse can also appear shallower than calculated with equation 4.11, if the planet does not re-emit all the energy it absorbs from its star. Absorption and emission from the planet's atmosphere will also effect the depth of the secondary eclipse at the corresponding wavelength.

The planet brightness temperature is derived as the temperature of a black body

with a total flux equivalent to the planet flux F_p , as follow:

$$T_B = \left(\frac{F_p}{4\pi\sigma_{SB}R_p^2} \right)^{1/4} \quad (4.12)$$

T_B is the true observable temperature from the eclipse depth calculated independently of any knowledge of the planet's thermal flux and the stellar reflected light components.

4.1.4 Variations of secondary eclipse's depth with R_p/R_* , a/R_* , A_B and f

The CoRoT bandpass is in the optical range, where both thermal emission and reflected light are expected to be significant contributions to the planet's flux. As these two components of the planet flux can not be disentangled with optical detection alone, the relation between the depth of the secondary and other parameters is investigated and the fraction of each component in each case extracted.

Method

The star is treated as a black body, and the stellar flux is calculated using Planck's law (equation 4.13) for a given stellar temperature (5800 K in the section). The stellar light reflected by the planet is calculated from the stellar black body using Equations 4.2 and 4.4. The planet is assumed to radiate like a black body and the planet thermal emission is calculated using Planck's law (equation 4.13) with a planet temperature calculated using Equation 4.10. The total flux of the planet is calculated as the sum of the stellar light reflected by the planet and the planet thermal emission.

The black body radiation follows the Planck's law:

$$F(\lambda) = \frac{2hc^2}{\lambda^5} \frac{1}{e^{\frac{hc}{\lambda kT}} - 1} \quad (4.13)$$

where $F(\lambda)$ is the flux intensity of the black body as a function of wavelength λ , h is the Planck constant, c is the speed of light, k is the Boltzmann constant, and T is the temperature of the black body.

All the fluxes are multiplied by the CoRoT response spectrum (Auvergne et al. 2009, wavelength range: (370,1000) nm), and the integral of each flux is calculated to give the total flux received within the CoRoT bandpass (F_* for the star, F_p for the planet). Figure 4.1 shows two examples ($A_B = 0.9$ and $A_B = 0.1$) of an implementation of stellar black body, stellar light reflected by the planet and planet black body view through the CoRoT bandpass. The depth of the secondary eclipse is calculated as $\frac{F_p}{F_*}$.

The lowest wavelength of the CoRoT red channel is calculated as the wavelength marking 60% of the total flux from the largest wavelength in the CoRoT bandpass, and the largest wavelength in the CoRoT blue channel as the wavelength marking 20% of

the total flux from the lowest wavelength in the CoRoT bandpass. These limits depend on the stellar temperature chosen; with the 5800 K chosen here the red channel is at (585,1000) nm, the green channel at (507,585) nm, and the blue channel at (370,507) nm). The planet and stellar fluxes in each of the CoRoT colour channels are calculated as the sum of the fluxes within the wavelength range associated to each channel.

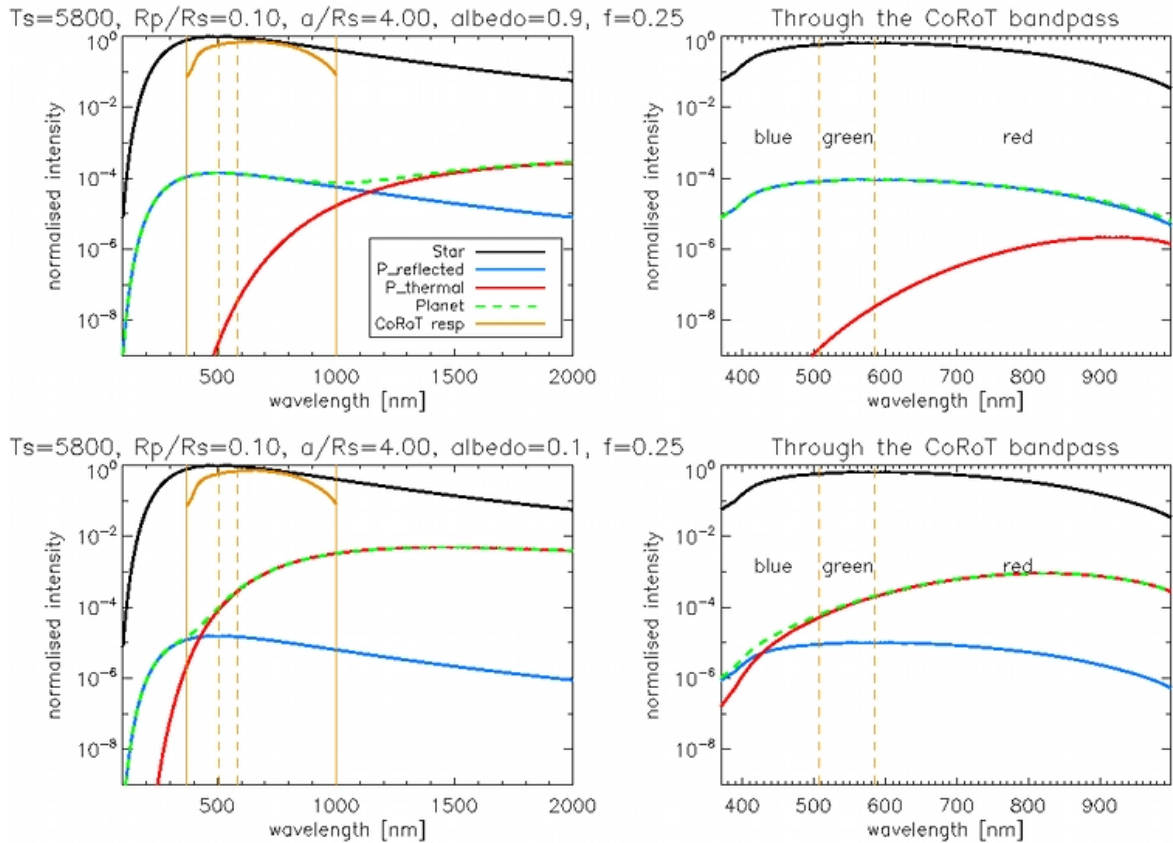


Figure 4.1: This figure shows the star emission (black) as a black body at 5800 K, and the planet emission (green dashed) composed of the stellar light reflected by the planet (blue) calculated as a fraction of the star emission (equations 4.2 and 4.4) and the planet thermal emission (red) derived as a black body at a temperature calculated with equation 4.10. The planet is set with $R_p/R_\star=0.1$ and $a/R_\star=4$, with an albedo $A_B = 0.9$ (top panels) or $A_B = 0.1$ (bottom panels), and a redistribution factor $f = 0.25$. The different emissions are multiplied by the CoRoT response spectrum (orange) and plotted in the right panels. The CoRoT bandpass is divided into red, green and blue channels defined as respectively containing 60%, 20% and 20% of the stellar flux within the CoRoT bandpass.

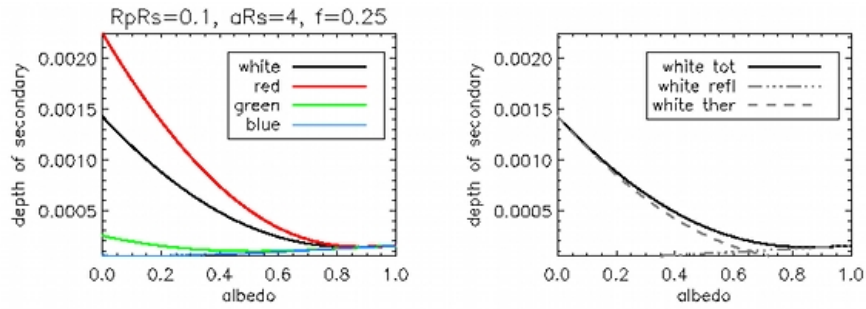


Figure 4.2: This figure shows the depth of the secondary eclipse $\frac{F_p}{F_\star}$ in the CoRoT bandpass (black), red channel (red), green channel (green) and blue channel (blue) for a 5800 K star and a planet with radius $R_p/R_\star=0.1$, orbital distance $a/R_\star=4$, redistribution factor $f=0.25$, and an albedo varied from 10^{-8} to 1. The depth of the eclipse taking into account only the reflected light (dash-dots grey) or only the thermal emission (dash grey) falling within the CoRoT bandpass is plotted in the right panel.

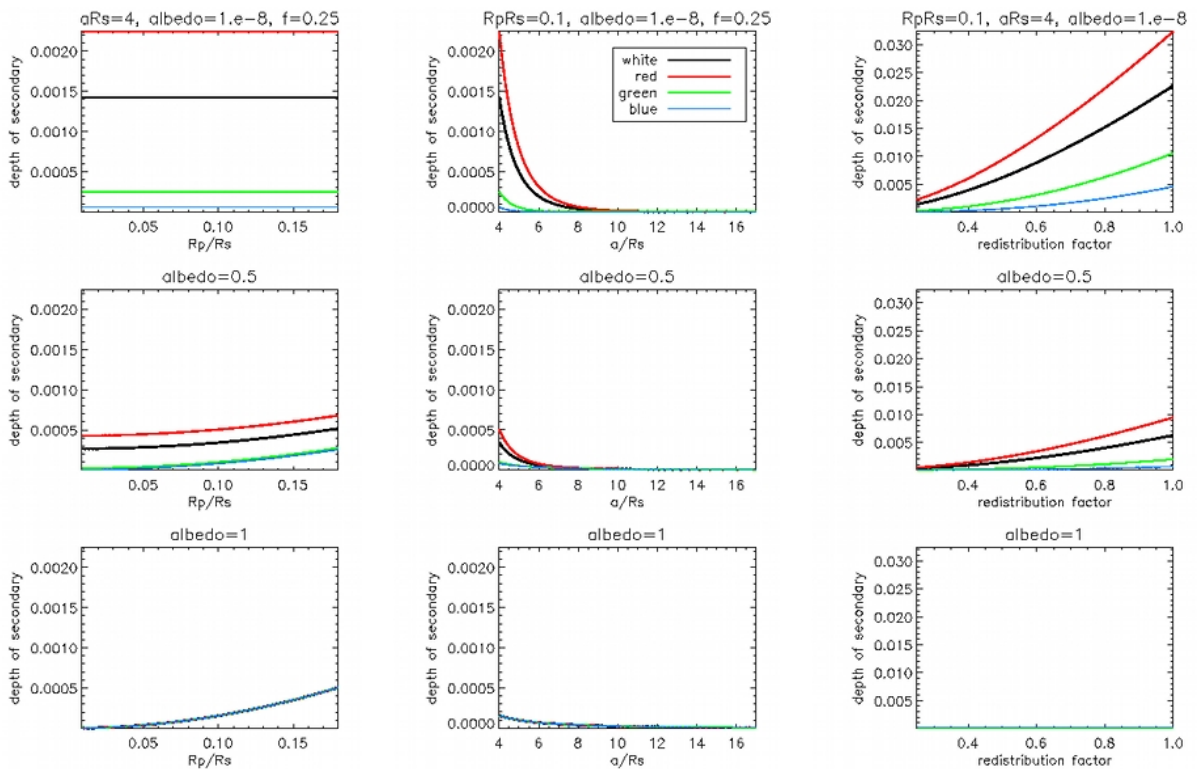


Figure 4.3: The depth of the secondary eclipse $\frac{F_p}{F_\star}$ of a planet around a 5800 K star is plotted for a range of planet radii R_p/R_\star (left column), a range of planet orbital distances a/R_\star (middle column), and a range of energy redistribution factor f (right column), and albedos of 10^{-8} (~ 0), 0.5 and 1 (from top to bottom). The depth is calculated for the stellar and planet fluxes falling within the CoRoT bandpass (black), the CoRoT red channel (red), green channel (green), and blue channel (blue).

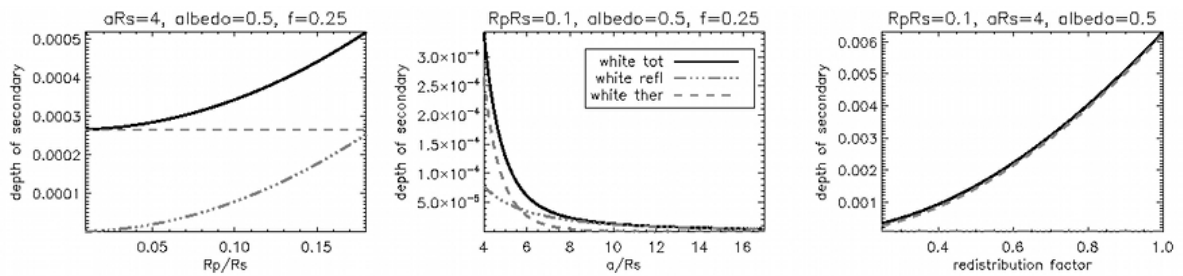


Figure 4.4: The black curves are the same as Figure 4.3 for albedo=0.5. The depth of the secondary over the CoRoT bandpass in stellar reflected light only (dash-dot) and in planet thermal emission only (dash) are plotted in grey.

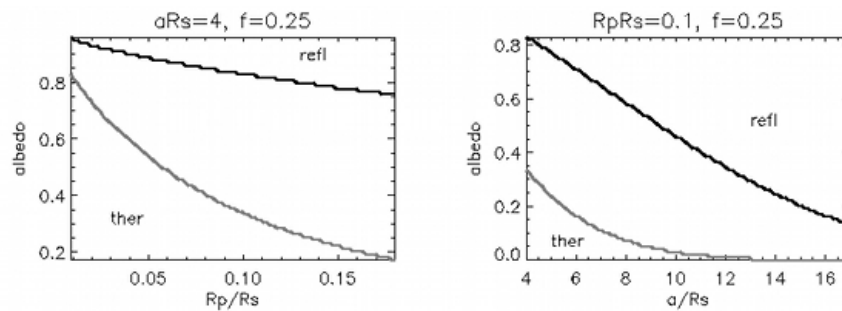


Figure 4.5: This figure shows which component of the planet emission dominates in the CoRoT bandpass depending on the albedo, the planet radius R_p/R_* and the planet orbital distance a/R_* , for a stellar T_{eff} fixed at 5800 K, and a planet redistribution factor fixed at 0.25. For this star-planet system, for (albedo, R_p/R_*) and (albedo, a/R_*) combinations below the grey line, the thermal emission is 10 times larger than the reflected light, and for combinations above the black line, the reflected light is 10 times larger than the thermal emission.

Several observations can be extracted from this analysis:

- At large albedos, the stellar light reflected by the planet dominates over the planet thermal flux and the flux ratio $\frac{F_p}{F_*}$ in the different CoRoT colour channels is the same. At small albedos (bottom panels), the planet thermal flux dominates over the reflected light and the flux ratio $\frac{F_p}{F_*}$ is larger in the red channel than in the blue channel (Figure 4.1 top panels; Figure 4.2 right panel; Figure 4.5). This can be used on secondary eclipses in the CoRoT light curves to test which type of emission dominates in the planet radiation.
- The planet to star flux ratio is a) larger in the red CoRoT channel than in the integrated CoRoT bandpass, b) similar in amplitude in the green and in the blue CoRoT channels but smaller than over the integrated CoRoT bandpass, c) mainly influenced, in the green and blue CoRoT channels, by the amount of stellar light reflected by the planet, and d) mainly influenced, in the red CoRoT channel, by the amount of thermal emission by the planet (Figure 4.2 left panel; Figure 4.3 top

6 panels).

- The maximum planet to star flux ratio is the highest when $A_B = 0$, has lower values at intermediate albedos between 0 and 1, and has another smaller local maximum at $A_B = 1$ (Figure 4.2; Figure 4.3).
- The planetary thermal emission (dominant component when $A_B \sim 0$) is independent of the radius of the planet R_p/R_* , decreases with the orbital distance a/R_* , and increases with the redistribution factor f (Figure 4.3; Figure 4.4 left panel)). This is as expected from Equation 4.10.
- The stellar light reflected by the planet (dominant component at $A_B \sim 0$) increases with the radius of the planet R_p/R_* , decreases with the orbital distance a/R_* , and is independent of the redistribution factor f (Figure 4.3; Figure 4.4). This is as expected from Equation 4.6.
- The planetary thermal emission and the stellar reflected light both drop with increasing orbital distance a/R_* , and the reflected light drops down to 0 at shorter orbital distance faster than the thermal emission (Figure 4.4 middle panel).
- The depth of the secondary eclipse increases with f (Figure 4.4 right panel), as the amount of observable thermal emission increases with f .
- The value of the albedo at which the stellar reflected light dominates ($10\times$ larger) over the planet thermal emission (like in Figure 4.2 right panel) decreases with R_p/R_* and a/R_* (Figure 4.5).

This study assumes that the planet is in thermal equilibrium, although in general some planets can be out of equilibrium, for instance due to chemical processes. Additionally, even if the planet is in global equilibrium, the depth of the secondary eclipse in a given band can differ strongly from the black body prediction because of the presence of strong absorbers in the atmosphere of the planet (e.g. hazes, molecules).

The absence of detection of optical secondary eclipses before those of CoRoT-1b and 2b (e.g. upper limits on HD209458b by MOST, Rowe et al. 2008) suggests that many Hot Jupiters typically have very low albedos (≤ 0.1).

4.1.5 Expected depth and phase for the secondary eclipse of CoRoT planets

From the equation 4.6 and 4.11, one can derive expected depths for the planet secondary eclipses if the planet flux is dominated by reflected flux or thermal emission respectively. These values are presented in Table 4.1. The values of the secondary depth are only upper limits if the planet flux is purely one type or the other. In the CoRoT optical bandpass we expect both contributions to be significant, so the values presented in Table 4.1 are not upper limits in the CoRoT band pass and should only be

used to give an order of magnitude of the secondary eclipse depth.

Table 4.1: Secondary eclipse depth $\Delta F/F$ and phase range ϕ_{sec} for the eight first CoRoT planets and CoRoT-3b, based on equations 4.6, 4.11 and 4.7. N_{tr} is the number of transits, i.e. the number of planet orbital period observed. σ_{2h} is the total noise over 2h in the CoRoT light curve before the stellar variability is filtered out, N_{2h} is the number of points in the light curve over 2h (13 points at 516s sampling).

	R_p/R_*	a/R_*	e	R ⁽¹⁾	N_{tr}	$\frac{\sigma_{2h}}{N_{2h}}$ ⁽²⁾	$\Delta F/F$ ⁽³⁾ $A_B = 1$	$\Delta F/F$ ⁽⁴⁾ $A_B = 0, f = 1$	ϕ_{sec}/P ⁽⁵⁾
CoRoT-1b	0.1433	4.92	0 ^(fixed)	13.4	38	$2.0 \cdot 10^{-3}$	$2.1 \cdot 10^{-4}$	$8.4 \cdot 10^{-4}$	0.5 ^(fixed)
CoRoT-2b	0.1622	6.34	0.03 ± 0.03	12.0	87	$1.4 \cdot 10^{-3}$	$1.6 \cdot 10^{-4}$	$6.4 \cdot 10^{-4}$	(0.481,0.519)
CoRoT-3b	0.0665	7.03	$0.008^{+0.015}_{-0.005}$	13.1	34	$1.9 \cdot 10^{-3}$	$0.2 \cdot 10^{-4}$	$0.8 \cdot 10^{-4}$	(0.493,0.507)
CoRoT-4b	0.1053	16.8	0.0 ± 0.1	13.4	6	$2.0 \cdot 10^{-3}$	$0.1 \cdot 10^{-4}$	$0.4 \cdot 10^{-4}$	(0.468,0.532)
CoRoT-5b	0.1120	8.97	$0.09^{+0.09}_{-0.04}$	13.8	27	$2.3 \cdot 10^{-3}$	$0.4 \cdot 10^{-4}$	$1.6 \cdot 10^{-4}$	(0.471,0.529)
CoRoT-6b	0.1162	16.8	<0.1	14.2	16	$2.5 \cdot 10^{-3}$	$0.1 \cdot 10^{-4}$	$0.4 \cdot 10^{-4}$	(0.468,0.532)
CoRoT-7b	0.0184	4.13	0.07 ± 0.07	11.4	153	$1.2 \cdot 10^{-3}$	$0.05 \cdot 10^{-4}$	$0.2 \cdot 10^{-4}$	(0.478,0.522)
CoRoT-8b	0.075	17.6	0 ^(fixed)	14.3	22	$2.5 \cdot 10^{-3}$	$0.1 \cdot 10^{-4}$	$0.4 \cdot 10^{-4}$	0.5 ^(fixed)
CoRoT-9b	0.115	93	0.11	13.8	1	$2.2 \cdot 10^{-3}$	$0.05 \cdot 10^{-4}$	$0.2 \cdot 10^{-4}$	(0.465,0.535)

The values of R_p/R_* , a/R_* and e for CoRoT-1b to 7b are taken planet parameter tables in Chapter 3 Section 3.2. The values for CoRoT-8b and 9b and taken from the planet discovery papers (Bordé et al. 2010, and Deeg et al. 2010 respectively).

⁽¹⁾ R is the magnitude of the planet's host star in the R filter. ⁽²⁾ σ_{2h} is calculated using equation 4.14. ⁽³⁾ Assuming the planet flux only comes from the stellar reflected light, using equation 4.6 and $A_B = 1$, this is an upper limit when the planet flux is dominated by the stellar reflected light. ⁽⁴⁾ Assuming the planet flux only comes from the planet thermal emission, using equation 4.11, $A_B = 0$ and $f = 1$. ⁽⁵⁾ ϕ_{sec} is derived using equation 4.7 for $\cos \omega = 0$ to 1.

Aigrain et al. (2009) derive the following empirical relations between the total noise over 2h (timescale comparable to the duration of a secondary eclipses) and the R-magnitude for dwarf stars:

$$\log \sigma_{2h} = 0.25 R + z \quad (4.14)$$

where z (~ -7 for the three first CoRoT fields) indicates the gradual degradation of CoRoT photometric performance over time – which can be associated with the increase in incidence of hot pixel events.

The value of $\frac{\sigma_{2h}}{N_{tr}}$ for each of the nine first CoRoT planets is reported in Table 4.1. The noise level in the unfiltered CoRoT light curve compared to the amplitude of the signal searched for in this chapter, illustrates the complexity of the task.

So far the smallest transit signal detected in the CoRoT light curves is the transit of CoRoT-7b with a depth of $3 \cdot 10^{-4}$. Thus, if we have enough orbits (large S/N), we can expect to detect in the phase-folded light curve the secondary eclipses of CoRoT-1b and 2b. The secondary eclipses of CoRoT-3b to 9b are expected to be too shallow to be detected in the CoRoT light curves. For these planets, a larger-diameter space telescope and more orbit coverage will increase the S/N of the secondary eclipse which might then become detectable depending on the level of systematics.

The expected range for the secondary eclipse of all the planets in Table 4.1 are between 0.45 and 0.56. The search for secondary eclipses is therefore run over the phase range (0.4,0.6).

Remarks

Some remarks can be made at this point:

- CoRoT broadband filter does not cover the whole wavelength range of the emission of the planet and the star (assumed in Table 4.1). To calculate the real expected depth of the secondary eclipses in the CoRoT optical band pass, one should thus convolute the Planck black body functions of the star ($4\pi R_\star^2 \sigma_{\text{SB}} T_\star^4$) and the planet ($4\pi R_p^2 \sigma_{\text{SB}} T_p^4$) with the CoRoT spectral response function given in Auvergne et al. (2009).
- F_p is a combination of $F_{\star, \text{reflected by planet}}$, $F_{p, \text{thermal emission}}$ and $F_{p, \text{internal}}$. At shorter wavelength, $F_{\star, \text{reflected by planet}}$ dominates and at longer wavelength $F_{p, \text{thermal emission}}$ dominates. In the CoRoT optical bandpass both contributions are significant. Therefore, for secondary eclipse detections in the CoRoT light curves, one can only give an upper limit on $T_{p, eq}$ as equal to the planet brightness temperature based on the assumptions of a total absorption of the stellar incident flux and a thermal equilibrium.
- Treating the planet thermal flux as a black body is an approximation as a planet spectrum has many and wide absorption features which results in the planet thermal flux being overestimated if approximated to a black body.

4.2 Method

In this section, I describe the methods used to process the CoRoT light curve and search for planet secondary eclipses and orbital phase variations in the white and colour channels.

4.2.1 The IRF as a reconstruction tool

As shown in Table 4.1, the noise level (mainly stellar variability) in the original CoRoT light curve of CoRoT-1b and CoRoT-2b is too high to allow the direct detection of a secondary eclipse. The light curves thus need to be filtered before searching for secondary eclipses. The IRF reconstructs all signals at the orbital period of the planet and is therefore an interesting tool to carefully filter the stellar variability from the original light curve. The IRF is described in Chapter 1 and applied in Chapter 2 to the CoRoT light curve of the first seven planets discovered by CoRoT. The IRF uses the knowledge

of the period of the transits to simultaneously estimate the transit signal and the stellar variability signal.

4.2.2 Light curve processing

The light curves are processed using the IRF as described in Chapter 3 Section 3.1.3. The amplitude of the signal searched for in this chapter is at least two order of magnitude smaller than the amplitude of the primary transit. The search for this signal is thus more sensitive to light curve discontinuities such as the sharp jumps in flux pointed out in Chapter 3. Several approaches can be taken to remove these flux discontinuities:

1. identify sections of the light curve around observed "jump" in flux, and work on the light curve excluding these sections. This approach is limited when using the IRF to filter large amplitude stellar variability (e.g. CoRoT-2). The IRF treats the whole light curve as a succession of points ignoring gaps in time. Thus if the flux level at the end of a chunk of the light curve is very different from the flux level at the start of the following chunk, the IRF will still see a sharp jump in flux at the transition between the two sections.
2. remove these jumps in flux directly with the IRF using larger `timescale` and `binsize` to smoothen out sharp jumps in flux in the unfolded light curve and phase-folded one respectively. This is a trade off as using a large `timescale` and `binsize` will be less efficient in estimating the stellar variability and the planet signal. Nevertheless, residuals of the jumps are still present at the 10^{-4} level.
3. therefore, the adopted approach is to filter the whole light curve with the IRF and post-filtering to cut out the planetary orbits which have a large jump in flux in the original light curve (typically 2 to 3 orbits over the whole light curve). This method works even for large amplitudes in stellar variability. If large jumps in flux are identified at the beginning and at the end of the light curve, the sections of light curve kept can start after the first jump and end before the second one (e.g. blue light curve of CoRoT-1), though caution should be used as keeping the maximum number of planet orbits increases the S/N of the planet secondary eclipse and the orbital phase variation.

The IRF-filtering is performed with `timescale` of 0.5 days or 0.25 days depending on the level of stellar activity. Choosing the correct `timescale` is important. If some stellar variability is kept and binned up in the transit signal, the residuals of this variability will then be present at all the planet orbits, "polluting" the orbits where the stellar signal was originally well estimated. This residual stellar variability is then more difficult to filter out as it is now at the planet orbital period, and the IRF will attempt to reconstruct it with the planet signal.

The values chosen for the IRF *binsize* parameter – used to estimate the transit-signal – are 0.01 or 0.005 phase units depending on how they model the transit – instead of 0.0006 phase units as used in Chapter 3. For small values of the IRF *timescale* parameter (< 0.25 day), the IRF starts decomposing the noise in the light curve into a component at the reconstructed period and a component filtered out (see Section 4.2.4 of this chapter for more explanation). To counter this effect, one needs to use a larger IRF *binsize* parameter so that the component of the noise kept at the reconstructed period is smoothed out in the transit signal estimate.

To avoid the issue of non-uniform weighting associated with non-uniform coverage of the phase-folded planetary orbit, which can bias the search for a secondary eclipse, only full planetary orbits are kept. The light curves searched for secondary eclipses are selected to start at first minimum and end at last minimum of IRF-filtered light curve (which correspond with good approximation to the centre of the first and the last transits in the light curve).

The resulting light curve is phase-folded at the orbital period of the satellite. If there is an apparent variation at this period (Figure 4.6), this signal is boxcar-smoothened and divided into the IRF-filtered light curve. The flux variations at the satellite orbital phase are due to the satellite entering and exiting the Earth’s shadow. The thermal shock at the exit of the Earth’s shadow and the change to battery power at the entry to the Earth’s shadow, cause pointing changes in the telescope. These variation have a 10^{-3} amplitude level which hinders the detection of secondary eclipses expected at a 10^{-4} level.

CoRoT has three colour channels which are added up together to create the white light curve (see Chapter 3 Section 3.1.2). The three colour channels, although with less photons and thus more photon noise than the white light curve, can be studied individually. This gives some colour information on the planet photometric signal. The individual colour light curves are processed in the same way as the white lights.

Over the light curves studied in this chapter, only the colour light curves (CoRoT red, blue and green channels) needed a correction at the satellite’s orbital period around the Earth. The white light curve was either corrected in the light curve production pipeline, or the effects average out when combining the three colours.

4.2.3 Search for secondary eclipses and orbital phase variations

Secondary eclipse

We searched the phase-folded IRF-filtered white light curves for secondary eclipses using a 2-parameter sliding box varying the phase and the total duration of the secondary eclipse. The duration is varied as an additional test of the reliability of the detection. The detection significance of each putative secondary eclipses is evaluated

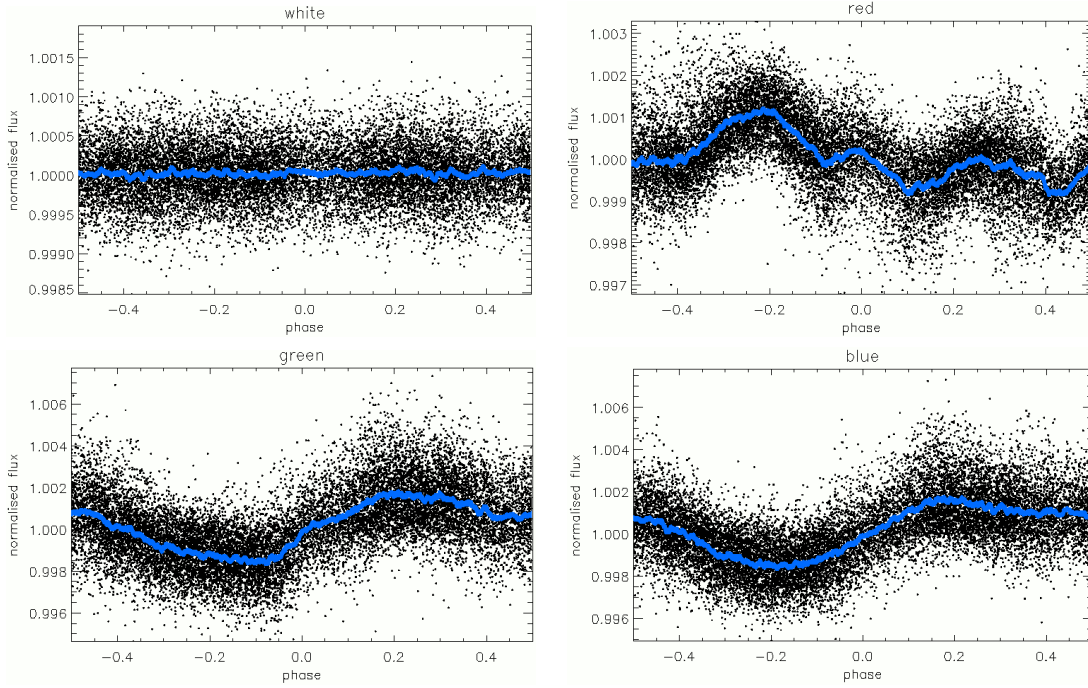


Figure 4.6: The white and colour light curves of CoRoT-2, IRF-filtered (timescale=0.25, timescale=0.005), and phase-folded at the orbital period of the CoRoT satellite around the Earth ($P \sim 103$ min). The blue curve is the smoothed version (bins of 100 points). The figure shows the variations at the period of the satellite.

as:

$$S = \frac{\delta}{\sigma_N} \quad (4.15)$$

where δ is the depth of the putative secondary eclipse and σ_N is the noise level for this putative secondary eclipse. $\delta = f_{\text{out}} - f_{\text{in}}$ where f_{in} and f_{out} are the median level in and out of transit respectively. f_{out} is calculated over the points between one and one-half the trial total-eclipse-duration from the trial phase. The duration-in-full-eclipse is derived for each trial eclipse-total-duration so that the ratio between the two is the same as that of the primary transit. f_{in} is calculated over the points within one-half the duration-in-full-eclipse from the trial phase, the number of points in this interval is called N . $\sigma_N = \sigma/N$ where σ is the $1.48 * \text{MAD}$ (MAD=median absolute deviation) of all the points one transit-total-duration away from the centre of the primary transit).

The phase of the secondary eclipse is varied from 0.4 to 0.6 phase units, for a primary transit centred at phase 0. The phase range is taken to cover the range of eccentricity determined with radial velocity measurements. The secondary eclipse total duration is varied from a quarter to twice the total duration of the primary transit. We perform the search for a secondary eclipse over a 100 to 200×100 to 200 grid in order to reach a sampling of the phase and the duration of 0.001 phase units.

The values of S at each trial phase and duration are combined into a 2-D significance map with in grey scale the value of the significance (white and black for high

and low values of S respectively). This map allows to visually evaluate the shape of the (phase,duration) parameter space with regards to the significance of the putative secondary eclipses. If the planetary orbit is circular, the secondary eclipse is expected at phase 0.5 with the same total duration as that of the primary transit.

If the phase-folded light curve is not flat around the putative secondary eclipse, a 1st or 2nd order polynomial fit is performed about each putative secondary eclipse before f_{out} and f_{in} are calculated.

The "best" secondary eclipse is the one with the highest significance S , and has an associated "best" phase and "best" duration.

For the same phase and duration as the secondary eclipse with the highest significance in the white light curve, the depth of the secondary eclipse in the different colour channels is estimated. The values are compared to the depth in the white light curve.

Trapeze model of the secondary eclipse with the highest significance

For the "best" secondary eclipse, a simple trapeze model is produced at the "best" phase with a total duration equal to the "best" duration, and an internal duration (planet fully eclipsed) with the same total to internal duration ratio as the transit. The in-full-eclipse level is calculated as the median of the points within the internal duration of the eclipse. The out-of-eclipse level is calculated as the median of the points in the range of $1\times$ to $1.5\times$ the "best" duration each side of the centre of the eclipse. This range was chosen as a compromise between being close enough to the eclipse to evaluate the local out-of-eclipse level, and far enough from the edge of the eclipse to avoid been biased by the eclipse.

Uncertainty on the depth of the secondary eclipse

The uncertainty on the depth can be calculated in the following ways:

1. as the 1σ dispersion ($1.48 * \text{MAD}$) of the points one transit-total-duration or more away from the centre of the primary transit, dividing this value by the square root of the number of points in-full-eclipse. This is how σ is calculated in the expression of the significance of the detection (equation 4.15). However, this method under estimates the uncertainty as it does not take into account the correlated noise in the phase-folded light curve.
2. residuals shuffled: as the 1σ dispersion ($1.48 * \text{MAD}$) of the depths of the secondary eclipse measured with different residual shuffling from the model of the "best" secondary eclipse S_{best} . This calculation is performed by subtracting S_{best} from the light curve, shuffling the residuals randomly, adding back S_{best} , and re-evaluating the depth of the secondary eclipse at the same phase and duration as S_{best} .

The above is done 100 times and the uncertainty on the depth are taken as the standard deviation of all the measured depths. However this method also underestimates the uncertainties as it treats the residuals as white noise and does not take into account any correlated noise present in the phase-folded IRF-filtered light curve.

3. residuals shifted: to take into account both the white and the correlated noise, the uncertainty on the depth can be estimated as in option (2) but with the residuals shifted circularly. Residual circular shuffling conserves the correlation between successive points, while residual random shuffling destroys it. This approach is the most conservative, i.e. should return the largest error bars. It is the one used in this chapter to evaluate the uncertainty on the depth of the secondary eclipse depth.
4. residuals permuted: the uncertainty on the depth can be estimated as in option (2) but with the residuals divided into bins of $\sim 1h$ and shuffled randomly. As each bin is shuffled as a whole, the detailed time sampling of individual bins is preserved. This method takes into account correlated noise on hour timescales.

Uncertainty on the phase and duration of the secondary eclipse

In the case of non-correlated noise, the 1 and 2 σ confidence level are respectively at $\Delta\chi^2 = 1$ and 2 from the minimum χ^2 . Here we also have correlated noise, so the above relation is not directly applicable.

For σ the uncertainty on the depth, the 1σ confidence level in the secondary eclipse phase is defined as the range in orbital phase where the depth is larger than the depth with the highest significance minus 1σ . The 2σ confidence level is defined where the depth is larger than the depth with the highest significance minus 2σ .

The 1σ and 2σ confidence levels in the secondary eclipse total-duration can be evaluated in the same way, i.e. by taking the range in eclipse total-duration where the depth is larger than the depth with the highest significance minus 1σ or 2σ respectively.

These 1σ and 2σ confidence level contours are plotted over the 2D-significance map of the search for a secondary eclipse in the phase-folded IRF-filtered light curve.

The 1σ uncertainty on the phase of the secondary eclipse is taken as the phase range of the 1σ confidence level, at the eclipse total-duration of the secondary eclipse with the highest significance. The 1σ uncertainty on the duration of the secondary eclipse is taken as the duration range corresponding to range within the 1σ confidence level and within the 1σ uncertainty phase range.

To consider a detection real, the depth of the secondary eclipse needs to be at least 2σ above the uncertainty associated with this depth. If the 1σ level in phase

includes phase 0.5 and the 1σ level in duration includes the duration of the primary transit, then the planet orbit is circular at a 1σ level.

Orbital phase variations

The amplitude of the orbital phase variation signal is of the same order of magnitude as that of the secondary eclipse. In theory, if a secondary eclipse is detected, an orbital phase variation can also be detected. In practice, systematics in the phase-folded light curve can easily reduce the significance of the detection of an orbital phase variation. Also, if the stellar variability has a residual component at the orbital period of the planet, it is difficult to separate this stellar signal from the planet orbital phase variation. Nevertheless, when a secondary eclipse is detected with at least a 2σ confidence level, we look in the phase-folded IRF-filtered light curves for sinusoidal flux variations at the planet orbital period that could be of planetary origin.

The filtered light curve is divided by the transit model and the secondary eclipse model. A 3σ clipping is performed on the resulting light curve to remove any large residuals from the models, with $\sigma = 1.48 * \text{MAD}$ of the transit-free and eclipse-free light curve. The resulting light curve is phase-folded at the orbital period of the planet and fitted by a sinusoid. The sinusoid fit is performed varying the half amplitude of the sinusoid (typically with 100 steps between 0.5 and $5 \cdot 10^{-4}$) and keeping the period fixed at the planet orbital period and the phase of the maximum fixed at the phase of the secondary eclipse. The best fit is identified as the one with the minimum χ^2 to the data. The current implementation of the planet orbital phase modelling makes two assumptions: 1) the phase variation is sinusoidal and 2) the hottest point on the planet is the point directly facing the star. In actual fact, this is not always true. The phase variation due to the planet thermal emission is sinusoidal, but the phase variation due to the stellar reflected light can deviate from the sinusoidal shape depending on the phase function of the reflective material at the surface of the planet. The maximum amplitude on the phase variation can deviate from the time of the secondary eclipse (i.e. the hottest point on the planet can deviate from the point directly facing the star) if there is a strong atmospheric circulation when observing the planet's thermal emission (e.g. HD189733b, Knutson et al. 2007a), or depending on the phase function of the reflective material at the surface of the planet when observing the planet in reflected light. The simplicity of the current implementation of the phase curve modelling is justified by the level of white noise and residual stellar variability observed in the filtered light curves studied in this chapter. In the near future, for planet phase curves not affected by stellar variability, the orbital phase modelling can be modified to allow the above parameters to vary.

The amplitude of the "best" sinusoid is compared to the amplitude of the planet flux which should be similar to the depth of the secondary eclipse estimated in Table 4.1. If the values are compatible within the error bar, the sinusoidal flux variation seen at the

orbital period of the planet is due to the planet orbital phases, and the amplitude of the sinusoid is a measure of the ratio of the night-side to the day-side of the planet.

The current model of the planet's orbital phase is not yet evaluated in a robust way, i.e. with appropriate confidence limits. The following approach to derive the uncertainty on this model will be implemented in the near future: 1) remove the best model of the planet photometric signature (transit + secondary eclipse + orbital phase variations) from the original unfiltered light curve, 2) shift the unfolded time array, 3) re-insert the best model of the planet photometric signature into the original unfiltered light curve, 4) re-filter the light curve with the IRF and re-evaluate the model of the orbital phase variation, 5) repeat many times (e.g. 100) and evaluate the uncertainty on the parameters of the planet's orbital phase model from the scatter in their value.

A model of the planet photometric orbit is obtained by multiplying together the transit model (Chapter 3, Section 3.2), the secondary eclipse model (Section 4.2.3) and the orbital phase model (this section).

This bootstrap method will evaluate the uncertainties of the orbital phase model take into account both the noise created by residual stellar activity and the noise created by the IRF. The noise created by the IRF is explained in Section 4.2.4.

4.2.4 Optimising the parameters of the IRF

The level of stellar variability hinders the detection of the secondary eclipse and orbital phase variations. The stellar signal is filtered out using the IRF. As the signal of interest is small in amplitude (~ 0.01 mmag), the filtering parameters of the IRF (timescale, binsize) need to be optimised to best filter each light curve. The analysis performed below presents a method to identify the best IRF filtering parameters for each light curve.

Method

The IRF is tested over timescale=(0.02, 0.05, 0.1, 0.2, 0.25, 0.5, 0.75, 1) days and binsize=(0.0005, 0.001, 0.005, 0.01) phase units, with a transit period chosen at 1.7423 days. The transits and eclipses are cut from the filtered light curve. The resulting dispersion of the points ($1.48 \cdot \text{MAD}$), and the amplitude of the variations in the binned phase-folded and corrected light curve are measured and compared to the values of the light curve pre-filtering.

A synthetic light curve is computed with a mean value of 1, a time coverage of 80 transit orbits, a time sampling of 512s, and white noise. The white noise is created from random selections from a Gaussian distribution with mean of 0 and standard deviation of 10^{-4} . The resulting simulated light curve with white noise only has a time coverage of 80 transit orbits (i.e. ~ 140 days, similar to CoRoT long runs). A truncated light curve with white noise only and a time coverage of 30 transit orbits (i.e. ~ 50 days, similar to CoRoT short runs) is created by taking the first 30 orbits of the previous synthetic light curve.

The IRF with different timescale and binsize is tested on these two white-noise-only light curves (Figure 4.7, top and bottom panels). Transits and secondary eclipses are then inserted at the transit period into the 30-orbits white-noise-only light curve, with transit and eclipse duration of 0.15 phase units, a transit depth of 10^{-3} and a secondary eclipse depth of 10^{-4} . The IRF is tested on this light curve (Figure 4.7, middle panels), and on the light curve of CoRoT-1 (Figure 4.8) and CoRoT-2 (Figure 4.9). On top of the white noise, the transits and the secondary eclipses, the light curve of CoRoT-1 has instrumental and environmental systematics and a low level of stellar variability, and the light curve of CoRoT-2 has a higher level of stellar variability.

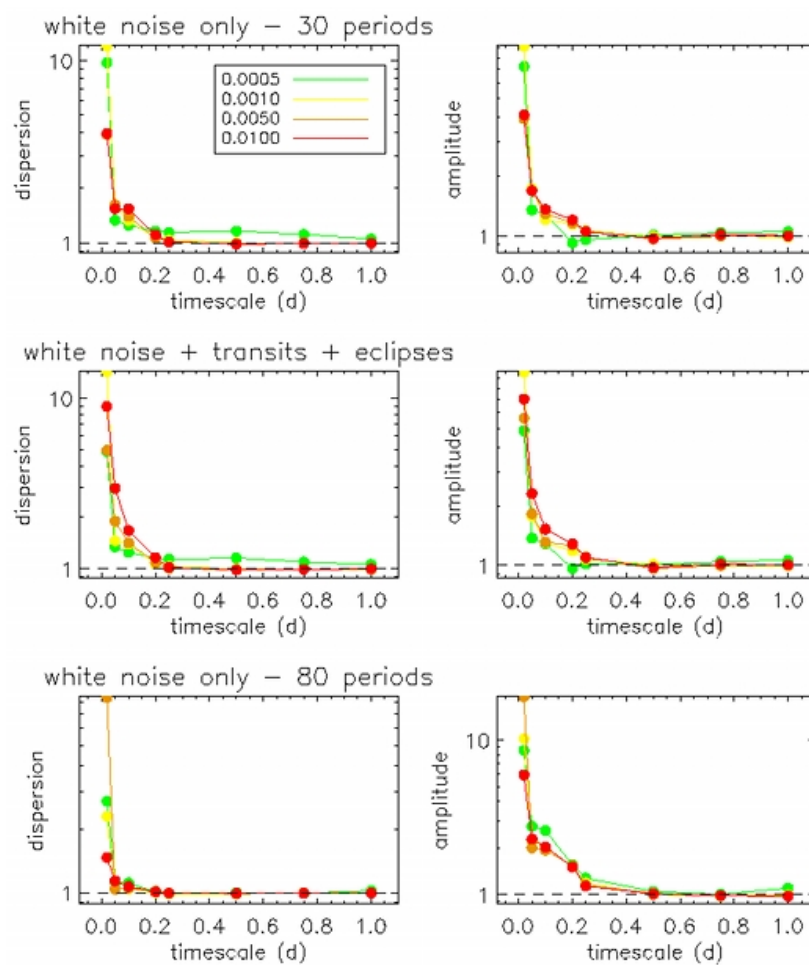


Figure 4.7: The IRF is tested with a range of timescale (x-axis) and binsize (green to red) on a simulated light curve over 30 planet orbits with white noise only (top panels) and with inserted transits and secondary eclipses (middle panel), and over 80 planet orbits with the same white noise component (bottom panels). The dispersion is calculated as the $1.48 \times \text{MAD}$ of the points in the filtered light curve compared to the original light curve (black dash line), and the amplitude is calculated as the minimum to maximum level of the phase-folded filtered light curve binned at 0.001 phase units with transit and eclipse cut out, compared to the same measurement in the original light curve.

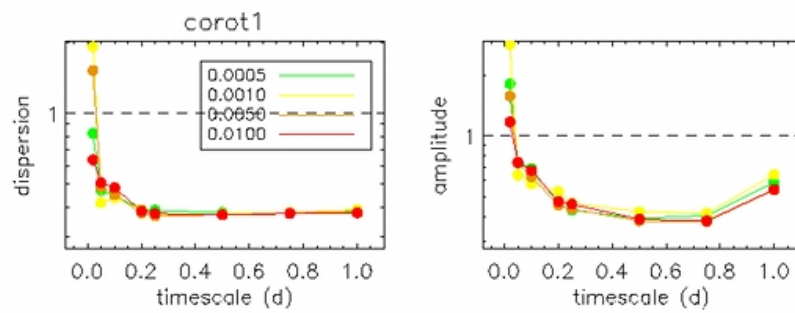


Figure 4.8: Same legend as Figure 4.7 but for the light curve of CoRoT-1.

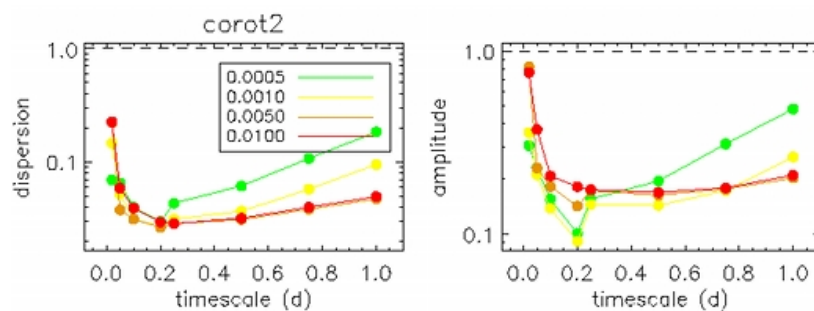


Figure 4.9: Same legend as Figure 4.7 but for the light curve of CoRoT-2.

Observations:

Based on the above analysis of figures 4.7, 4.8 and 4.9:

- In the case of the white noise only, the dispersion and the amplitude of the points in the filtered light curve increase suddenly for timescale lower than 0.2. In general, a large binsize (0.01) provides a lower increase in dispersion and amplitude as it smoothens out features in the phase-folded light curve during the filtering. The increase in dispersion and amplitude at small timescale is due to the fact that for these timescale the IRF has very few points per smoothing length, and through iterative smoothing and binning, it creates and emphasizes features picked up from the binned white noise.
- Adding transits and eclipses does not change the behaviour above timescale = 0.2, but for timescale smaller than 0.2 the dispersion and amplitude are larger at large binsize. The additional increase in the dispersion and amplitude at small timescale and large binsize is due to the edges of the phase-folded transit and eclipse affecting the value of the surrounding bins.
- Having a time coverage of 80 orbits – instead of 30 – gives similar results for the amplitude (sudden increase for timescale smaller than 0.25) but allows for smaller

timescale (0.05) with a small dispersion. This is because with more orbits, the noise averages out better in the phase-folded light curve and less features are picked up from the binned noise.

- In the case of CoRoT-1, down to $\text{timescale} = 0.1$, the dispersion and the amplitude are smaller in the filtered light curve than in the original light curve; this is because most of the stellar variability has been filtered out. The amplitude is the lowest at $\text{timescale} \sim 0.5$ then increases, the dispersion is constant until $\text{timescale} \sim 0.2$ then increases, and down to $\text{timescale} = 0.2$ a large $\text{binsize} (0.01)$ gives a lower dispersion and amplitude; these are for the same reason as the first and second points.

A low dispersion means a low level of residual noise and a low amplitude means small correlated residuals. The optimal set of IRF parameters occurs when both the dispersion and the amplitude are at their minimum. In the case of the transit light curve of CoRoT-1b, this is found at $\text{timescale} = 0.5$ and $\text{binsize} = 0.01$.

- CoRoT-2: With the same logic as the previous point, the optimal set of IRF parameters in the case of transit light curve of CoRoT-2b is for $\text{timescale} = 0.2$ and $\text{binsize} = 0.001$.

However, in practice for this planet (section 4.3.2) timescale of 0.25 and 0.5 and binsize of 0.005 and 0.01 are used as they give a flux modulation at the planet orbital period more consistent in shape with the flux variation due to the planet orbital phases.

4.3 Application to CoRoT planets

In this section, the IRF is used to filter the white and colour light curves of CoRoT-1 and CoRoT-2. The search for secondary eclipses and orbital phase variations are then performed on the phase-folded light curves. The results are compared with the discovery papers of the secondary eclipses of these planets.

4.3.1 CoRoT-1b

The detection of the secondary eclipse and the orbital phase variation of CoRoT-1b in the red channel of CoRoT was published in Snellen et al. (2009a). An independent measurement of the secondary eclipse of CoRoT-1b in the CoRoT white light curve was also published in Alonso et al. (2009a).

The white and colour light curves are processed as described in section 4.2.2. The search for a secondary eclipse and an orbital phase variation in the white and colour light curves is performed as described in sections 4.2.3 and 4.2.3.

Secondary eclipse and orbital phase variation in the white light curve

The IRF-filtering is performed with timescale of 0.5 and binsize of 0.01. After filtering, two orbits affected by sudden jumps are cut from the analysis (Figure 4.10).

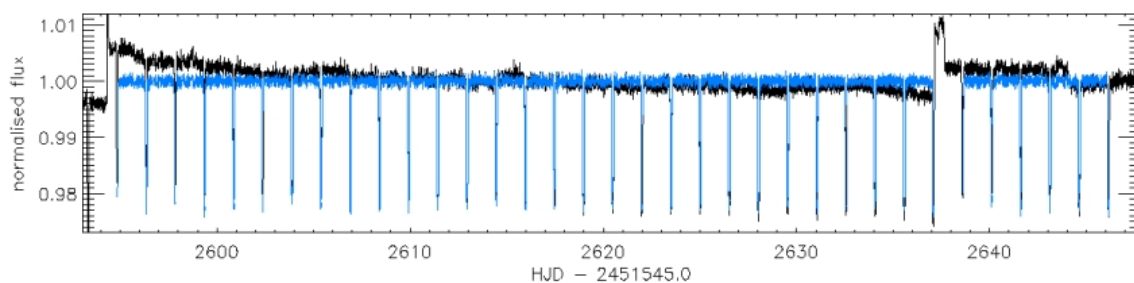


Figure 4.10: CoRoT-1 original white light curve with outliers removed (black) and its IRF-filtered version (blue) on which the secondary eclipse search is performed.

The search for a secondary eclipse is performed on the phase-folded white transit light curve of CoRoT-1b (blue, Figure 4.10) in a grid of 200×100 over the phase range (0.4,0.6) and the duration range (0.018,0.145) phase units.

Figure 4.11 shows the map of the significance of detection at each trial phase and duration. The secondary eclipse with the highest significance is at phase 0.500 and duration 0.066, and has a depth of $2.9 \cdot 10^{-4}$. Figure 4.12 shows the binned phase-folded transit light curve with the secondary eclipse model with the highest significance. The uncertainty on the depth is $0.8 \cdot 10^{-4}$, calculated as described in section 4.2.3; this corresponds to a detection of the secondary eclipse of CoRoT-1b at 3.6σ .

The 1σ and 2σ levels are plotted in Figures 4.11 as the level where the depths of the putative secondary eclipses are 1σ and 2σ respectively smaller than that of the secondary with the highest significance. The phase range associated to the 1σ confidence levels is measured in Figure 4.11 (bottom), and corresponds to (0.481,0.505). The duration range associated to the 1σ phase range is measured in Figure 4.11 (top), and corresponds to (0.042,0.091) in phase units. The total duration of the primary transit is 0.072 in phase units, therefore the duration of the secondary eclipse is compatible with that of the primary transit at a 1σ level.

In Figure 4.11 (top), the features at the 1 and 2 σ levels at duration shorter than 0.04 phase units are due to correlated noise. For duration at time scales close to that of the correlated noise, the search algorithm detects features of significant amplitude, though at longer duration the amplitude of these features average out. These correlated noise features are disregarded when evaluating the 1σ ranges in phase and duration.

The fit to the orbital phase variation is performed as in section 4.2.3. 74 outliers (out of 7026 data points) are clipped out by a 3σ clipping (where σ is the dispersion of the points out of transits). The amplitude found for the orbital phase variation is $2.1 \cdot 10^{-4}$ (as shown in Figure 4.12) which is compatible with the planet to star flux ratio estimated in Table 4.1 and with the depth of the secondary eclipse measured in this section.

Analysis of the colour channels

The red light curve of CoRoT-1 is filtered with the IRF using $\text{timescale} = 0.25$ and $\text{binsize} = 0.01$, the green light curve with $\text{timescale} = 0.5$ and $\text{binsize} = 0.005$, and the blue light curve with $\text{timescale} = 0.5$ and $\text{binsize} = 0.01$. In the case of the blue channel, the filtering is done only over the middle section of the light curve (2595 to 2637 days in CoRoT's date) as the start and the end of the blue light curve are affected by sudden jumps in flux. Three orbits are affected by a sudden discontinuity in flux and are cut out in the green channel after filtering. The three IRF-filtered colour light curves are then corrected from the flux variations at the satellite's orbital period (due to the crossing of the Earth's shadow).

The depth of the secondary eclipse in each colour is measured at the same phase and duration as the secondary eclipse with the largest significance in the white light curve. The uncertainty on the depth in each colour channel is derived as the standard deviation of the depth measured with the residuals shuffled circularly. The measured depths are $(2.0 \pm 1.0) \cdot 10^{-4}$ in red, $(3.1 \pm 1.9) \cdot 10^{-4}$ in green, and $(2.7 \pm 2.4) \cdot 10^{-4}$ in blue.

The orbital phase modulation is measured as $3.0 \cdot 10^{-4}$ in the red light curve, larger but compatible with the depth of the secondary eclipse in red. In the blue and green light curves, the noise level – mainly due to the photon noise as these channels receive 3 times less flux than the red channel – is too large to measure a significant orbital phase modulation.

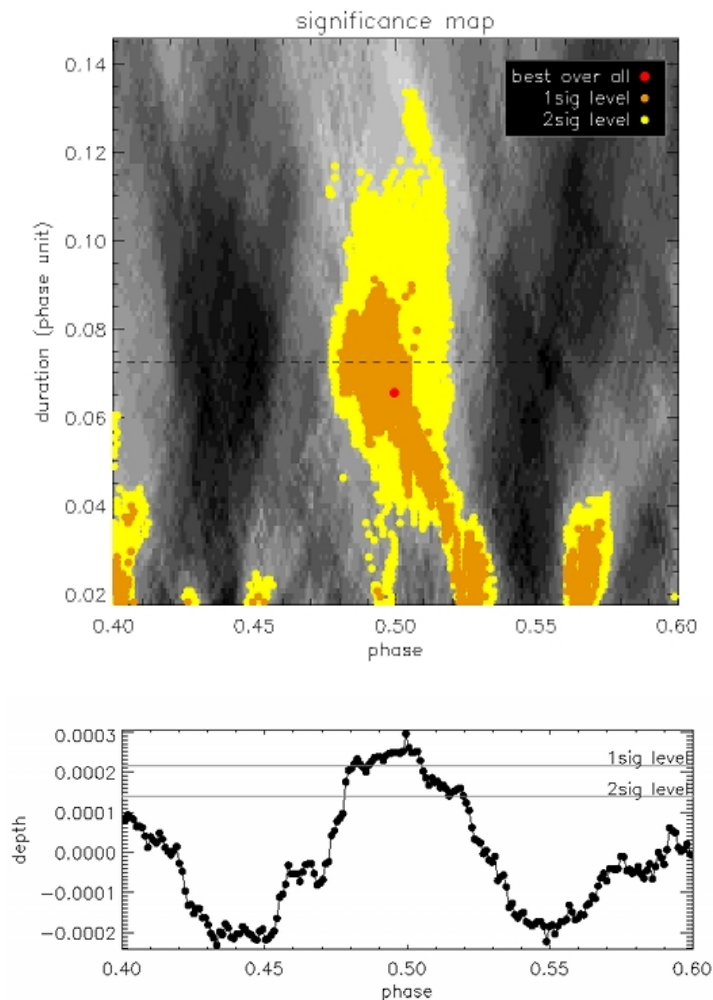


Figure 4.11: Top panel: Detection significance map displaying the significance of putative secondary eclipse of CoRoT-1b at different phases and duration calculated with equation 4.15 (darker grey indicating lower significance) in the IRF-filtered white light curve. The red dot is the best secondary, i.e. with the highest significance. The orange and yellow regions are the putative secondaries with depth within 1 and 2σ respectively of the depth of the best secondary (σ being the uncertainty on the depth of the best secondary). The black dashed line marks the duration of the primary transit. The significance goes down either side of the maximum as the out-of-eclipse window used to evaluate the out-of-eclipse level falls in the actual eclipse, thus returning a shallower depth of putative eclipse. Bottom panel: Depth of the putative secondary eclipses of CoRoT-1b (white light curve) as a function of phase and for a total duration fixed at that of the secondary with the highest significance. The highest peak shows the depth and phase of the best secondary eclipse. The grey lines show the 1 and 2σ confidence levels defined as in the top figure.

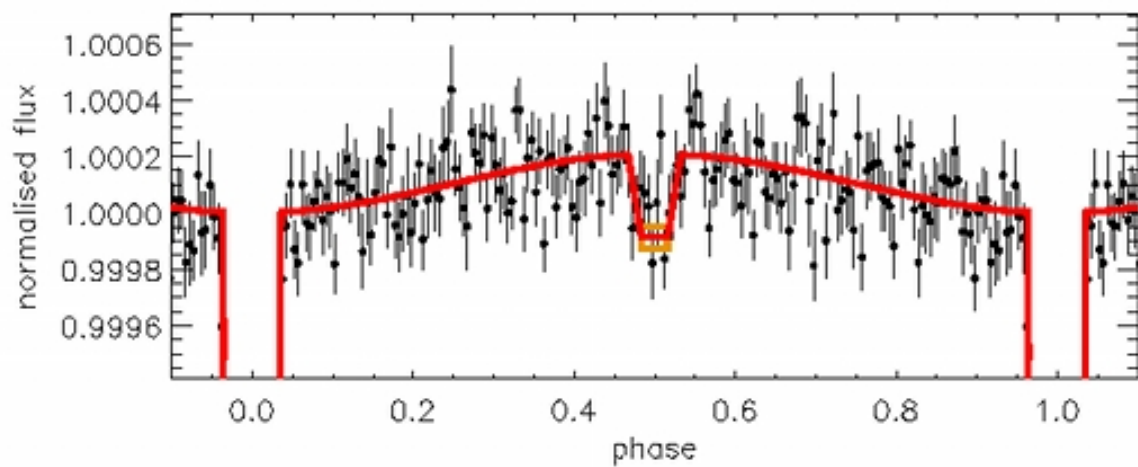


Figure 4.12: The phase-folded white transit light curve of CoRoT-1b binned with a bin size of 0.005 phase units (black), with the planet photometric orbit in red. The photometric orbit contains a models of the primary transit, a model of the secondary eclipse (the uncertainty on the secondary eclipse depth is marked with orange lines) and a model of the orbital phase variations. The model of the secondary eclipse is a trapeze at phase 0.5 with a total duration of 0.066 phase units, an internal duration (planet fully eclipsed) with the same duration ratio as the transit, and a depth of $(2.9 \pm 0.8) 10^{-4}$. The model of the orbital phase variation is a sinusoid with an amplitude of $2.1 10^{-4}$, a period fixed to the planet orbital period and a phase at maximum amplitude fixed to the phase of the secondary eclipse.

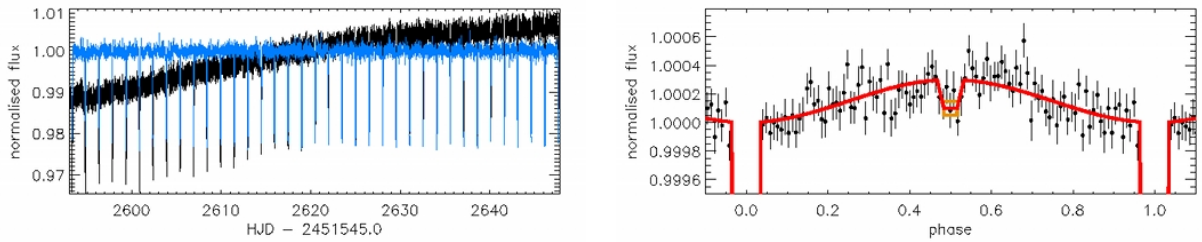


Figure 4.13: Red channel of CoRoT-1. The legend is the same as Figure 4.10 (left panel) and 4.12 (right panel). The phase-folded light curve is binned (bins of 0.009 phase units) for clarity of display. The phase and duration of the secondary eclipse is fixed to the detection with the highest significance in the white light curve. In the red channel, the depth of the secondary eclipse is $(2.0 \pm 1.0) 10^{-4}$ and the amplitude of the best fit sinusoid to the orbital modulation is $3.0 10^{-4}$.

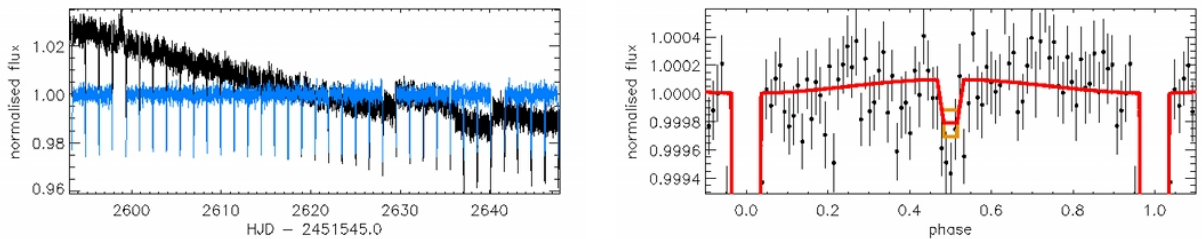


Figure 4.14: Green channel of CoRoT-1. The legend is the same as Figure 4.13. The phase-folded light curve is binned (bins of 0.011 phase units) for clarity of display. In the green channel, the depth of the secondary eclipse $((3.1 \pm 1.9) 10^{-4})$ is largely affected by the noise level and the amplitude of the best fit sinusoid to the orbital modulation $(1.0 10^{-4})$ is negligible within the noise.

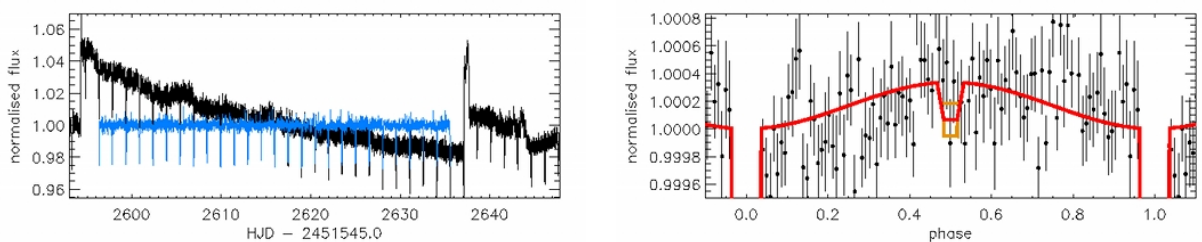


Figure 4.15: Blue channel of CoRoT-1. The legend is the same as Figure 4.13. In the blue channel, the depth of the secondary eclipse $((2.7 \pm 2.4) 10^{-4})$ and the amplitude of the best fit sinusoid to the orbital modulation $(3.4 10^{-4})$ are negligible within the noise.

Results

A convincing detection of the secondary eclipse of CoRoT-1b, and to some extent of its orbital variation, were achieved in the IRF-filtered CoRoT white light curve. The measurements are summarised in Table 4.2. The phase and duration are compatible with a planet circular orbit at a 1σ level. The depth is compatible within 1σ with the depth for an emission purely in reflected light (Table 4.1), but the depth is larger suggesting that there is a component of planet thermal emission within the planet flux which is in favour of an albedo $A_B < 1$. In the white light curve, a phase modulation is observed. The amplitude of the orbital phase variation in the white channel suggests a bright day side and a dark night side with a small redistribution of the energy between the two (small f).

At the same phase and duration as the secondary eclipse in the white light curve, the depth of the secondary eclipse of CoRoT-1b in the red channel is measured at $(2.0 \pm 1.0) 10^{-4}$,

The precision at which the depths of the secondary eclipse of CoRoT-1b are measured in the green and blue channels does not allow us to differentiate between a planet emission dominated by the reflected light (in which case we would observe the same secondary eclipse depth in the three colour channels) and a planet emission dominated by thermal radiation (in which case we would have observed a larger depth in the red channel than in the blue and white light curves).

In the case of CoRoT-1b, the detection of its secondary eclipse and orbital phase variation with a large signal to noise ratio, is limited by the photon noise.

Table 4.2: Summary table of the secondary eclipse depths and phase modulation of CoRoT-1b in the different colour channels of CoRoT

	white	red	green	blue	theoretical ⁽¹⁾	
					$A_B = 1$	$A_B = 0$ $f = 1$
Phase	$0.500^{+0.005}_{-0.019}$	same ^(fixed)	same ^(fixed)	same ^(fixed)	0.5 ^(fixed)	
Duration	$0.066^{+0.023}_{-0.026}$	same ^(fixed)	same ^(fixed)	same ^(fixed)		
Depth	$(2.9 \pm 0.8) 10^{-4}$	$(2.0 \pm 1.0) 10^{-4}$	$(3.1 \pm 1.9) 10^{-4}$	$(2.7 \pm 2.4) 10^{-4}$	$2.1 10^{-4}$	$8.4 10^{-4}$
Phase variation	$2.1 10^{-4}$	$3.0 10^{-4}$	-	-		

The phase and duration are expressed in phase units.

⁽¹⁾ from Table 4.1

4.3.2 CoRoT-2b

The detection of the secondary eclipse of CoRoT-2b in the white CoRoT light curve was first published in Alonso et al. (2009b). An independent measurement of its secondary eclipse in the red CoRoT light curve was published in Snellen et al. (2009b).

Search for secondary eclipse and orbital phase variation in the white light curve

To keep a uniform coverage of the planet orbital period and the stellar rotation period, only the first 24 full planet orbits are selected in the white light curve – 24 is a multiple of the planet orbital period and the stellar rotation period (4.5-5 days, Alonso et al. 2008). The IRF is then applied to this section of the CoRoT-2 white light curve, using $\text{timescale} = 0.25$ and $\text{binsize} = 0.005$ (Figure 4.16).

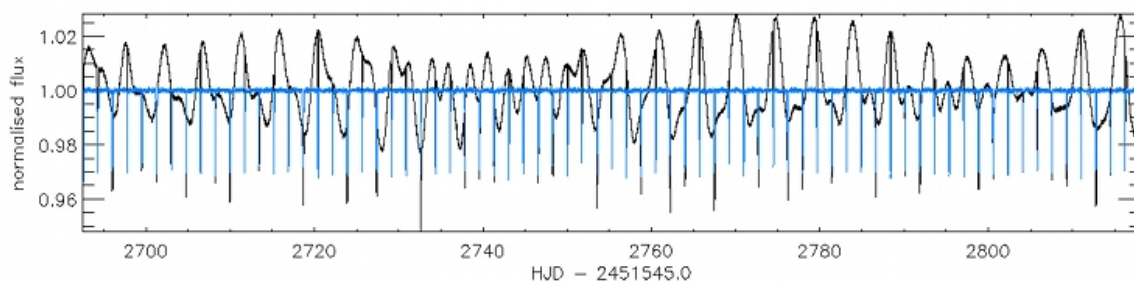


Figure 4.16: The 24 first planet periods of the white light curve of CoRoT-2 (black) and the IRF-filtered version (blue).

The search for a secondary eclipse is performed over a grid of 200×100 with a phase range of (0.4,0.6) and a duration range of (0.014,0.110) phase units.

The detection significance map is plotted in Figure 4.17. The secondary eclipse with the highest significance is at phase 0.496 and duration 0.071 phase units, and has a depth of $8 \cdot 10^{-5}$ (plotted in Figure 4.18). The uncertainty on the depth is $1 \cdot 10^{-5}$, calculated as described in the section 4.2.3. This value seems underestimated compared to the visual evaluation of the residuals in the light curve. However, as we know where to expect the secondary eclipse and at which duration, the search window has been reduced and the level of systematics is lower within that window. A robust determination of the residuals would include the systematics outside the searched range in phase, in which case the detection of CoRoT-2b in the current light curve would be unsuccessful.

The phase range associated to the 1σ confidence levels corresponds to (0.482,0.501) and the associated duration range is (0.041,0.082) phase units.

The sinusoidal fit to the modulation at the planet orbital period is performed as described in Sections 4.2.3 and 4.3.1. The amplitude of the orbital modulation in the IRF-filtered white light curve of CoRoT-2 is measured at $14 \cdot 10^{-5}$ (plotted in Figure 4.18).

Analysis of the colour channels

The red and green light curve of CoRoT-2 are filtered with IRF timescale = 0.25 and binsize = 0.01, and the blue one with timescale = 0.5 and binsize = 0.01. The filtered light curves are corrected from the flux modulation at the period of the satellite. These modulations are seen to evolve over the CoRoT light curve (probably due to residual stellar variability), and are modelled and corrected using individual chunks of two planetary orbital periods – instead of over the whole light curve all at once.

In each processed colour light curve, the depth of the secondary eclipse is measured at the same phase and duration as the secondary eclipse in the white light curve. The secondary eclipse in the different colours are plotted in Figures 4.19, 4.20 and 4.21, and are summarised in Table 4.3.

Results

At a 1σ level, the duration of the secondary eclipse is compatible with that of the primary transit (0.055 phase units) and the phase of the secondary eclipse is compatible with phase 0.5. The orbit of CoRoT-2b is thus compatible with a circular orbit.

The depth of the secondary eclipse measured in the white light curve is smaller than the maximum values calculated in Table 4.1, meaning that in the CoRoT bandpass, the planetary flux is composed of both reflected and thermal emission.

The depth of the secondary eclipse in the red channel is compatible with the one found in the white channel.

No secondary eclipses are observed in the green and blue light curves at a level larger than the noise estimated at $3\text{--}5 \cdot 10^{-5}$. This can be associated to the smaller amount of flux in these two channels compared to the red channel.

The value of the orbital modulation in the IRF-filtered light curves of CoRoT-2 are larger than the associated depths of the secondary eclipses. They are likely due to residual stellar variability at the orbital period of the planet, and not the the planet itself.

Table 4.3: CoRoT-2b secondary eclipse: summary of results

	white	red	green	blue	theoretical ⁽¹⁾	
					$A_B = 1$	$A_B = 0$
					$f = 1$	
phase	0.496 ^{+0.005} _{-0.014}	same ^(fixed)	same ^(fixed)	same ^(fixed)	(0.481, 0.519)	
duration	0.071 ^{+0.011} _{-0.030}	same ^(fixed)	same ^(fixed)	same ^(fixed)		
depth	$(8 \pm 1) \cdot 10^{-5}$	$(5 \pm 3) \cdot 10^{-5}$	-	-	$1.6 \cdot 10^{-4}$	$6.4 \cdot 10^{-4}$

The phase and duration are expressed in phase units.

⁽¹⁾ from Table 4.1

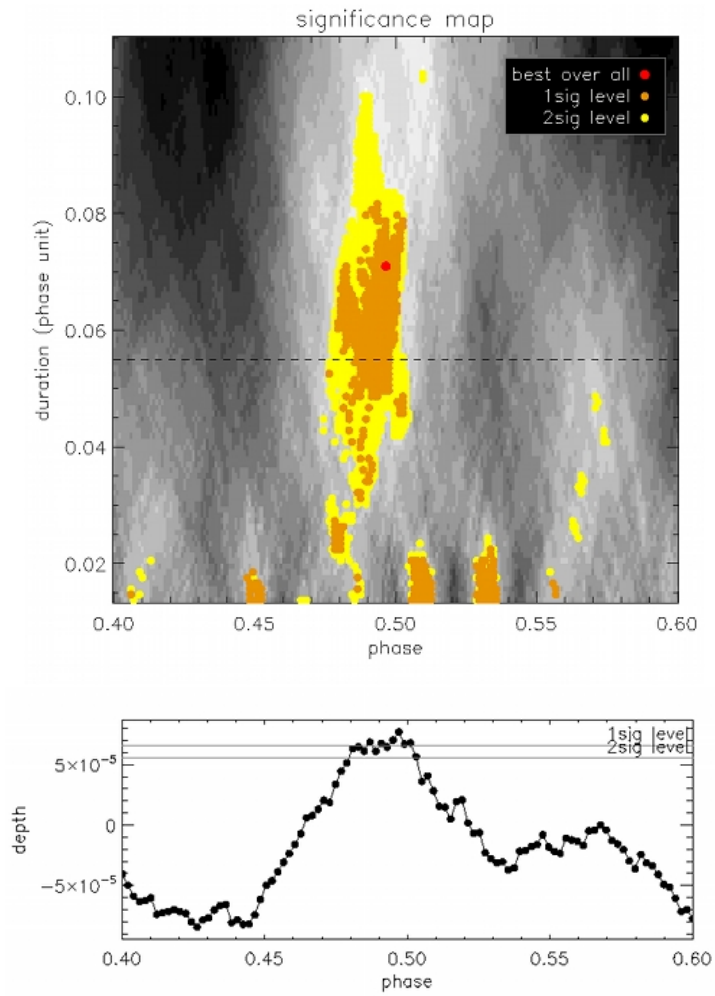


Figure 4.17: Search for a secondary eclipse in the phase folded white light curve of CoRoT-2. Same legend as Figure 4.11.

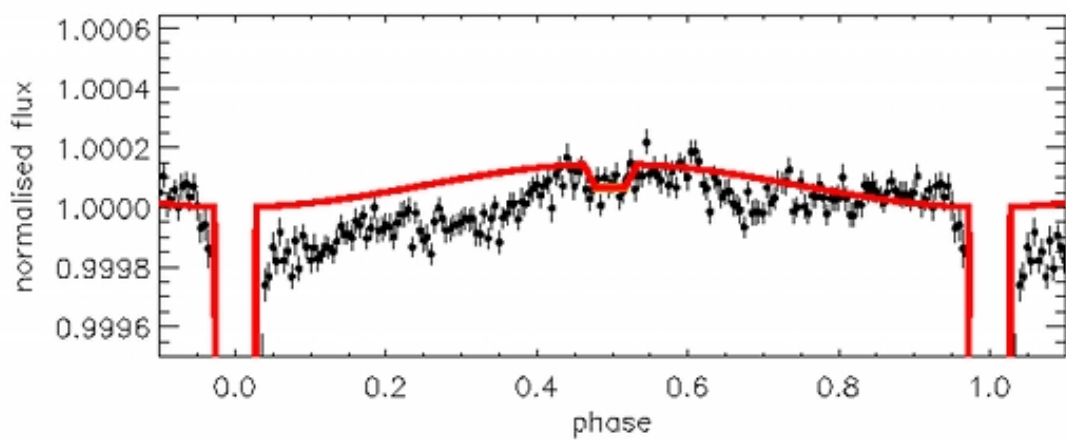


Figure 4.18: Model of the secondary eclipse and the phase modulation of CoRoT-2b (red). Same legend as Figure 4.12.

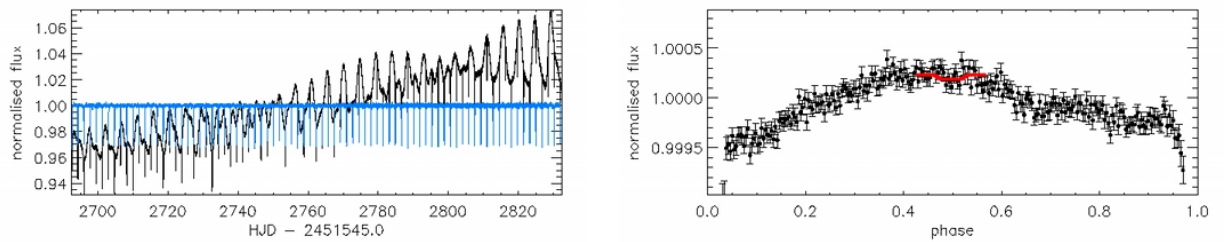


Figure 4.19: Red channel of CoRoT-2 (left, black) and IRF-filtered version (left, blue) phase-folded and binned on the right. The depth of the secondary eclipse in the red light curve, at the same phase and duration as in the white light curve, is $(5 \pm 3) 10^{-5}$ (model in red). The modulation at the planet orbital period is 10 times larger than the depth of the secondary eclipse due to residual stellar variability at the orbital period of the planet.

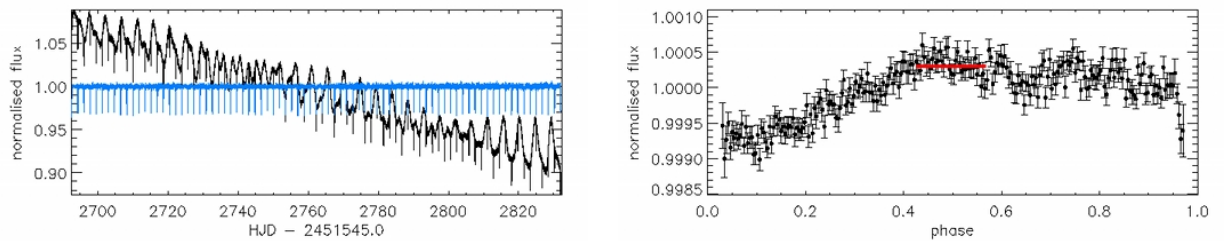


Figure 4.20: Green channel of CoRoT-2. Same legend as Figure 4.19. No secondary eclipse is detected in the green light curve at a level larger than the noise level ($3 10^{-5}$).

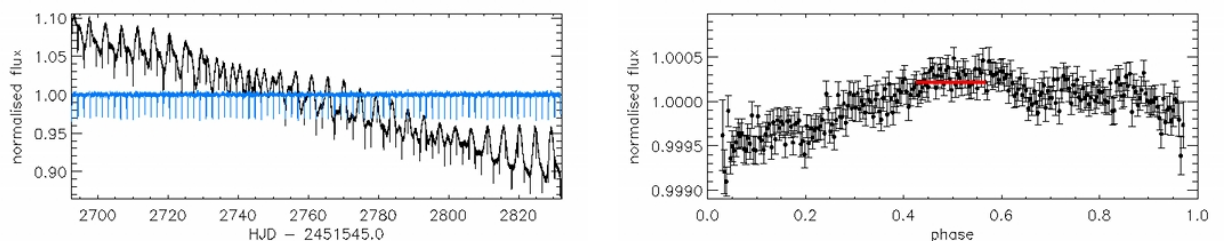


Figure 4.21: Blue channel of CoRoT-2. Same legend as Figure 4.19. No secondary eclipse is detected in the blue light curve at a level larger than the noise level ($5 10^{-5}$).

4.4 Discussion

4.4.1 Comparison with the literature

The secondary eclipse of CoRoT-1b was detected at 4σ . The value found for the depth in the white light curve is larger but compatible within 2σ with the $1.6\pm 0.6 \cdot 10^{-4}$ measured by Alonso et al. (2009a) in the white light curve. The phase modulation of the planet was observed here in the IRF-filtered white light curve, though this detection was not achieved in Alonso et al. (2009a) due to differences in light curve processing. Observing the planetary phase modulations in the IRF-filtered light curve shows the high quality of the light curve processing. The depth of the secondary eclipse in the CoRoT red channel is compatible within 1σ with the $1.26\pm 0.33 \cdot 10^{-4}$ measured by Snellen et al. (2009a) in the red light curve. A modulation in phase in the red channel is also observed, as in Snellen et al. (2009a). The difference between Snellen's analysis and this one is in the processing of the light curve and the modelling of the signal. Snellen modelled the depth of the secondary eclipse as the difference between the maximum of the phase variations and the night emission (which he modelled as zero), while in this chapter the transit depth was measured without accounting for a zero-level night emission. This means that the method described in this chapter can derive deeper secondary eclipse's depth than Snellen's method, simply from the choice of planet orbital variation modelling (i.e. modelling the planet night side emission simultaneously or not).

The secondary eclipse of CoRoT-1b was also observed in the K-band by (Rogers et al., 2009) and Gillon et al. (2009) (narrower band). Figure 4.22 presents these measurements compared to the ones in the CoRoT bandpass as published in the literature and as derived in this chapter. As expected, the depth of the secondary eclipse in the optical is smaller than in the infrared.

The secondary eclipse of CoRoT-2b was observed with a much lower confidence level than CoRoT-1b due to the level of residual stellar variability at the orbital period of the planet. Nevertheless, this value of secondary eclipse depth is compatible within 1σ with the measurement by Alonso et al. (2009b). The depth in the red channel is 2σ smaller than the value published in Snellen et al. (2009b). The difference in the values is expected to come from the difference in light curve processing.

The secondary eclipse of CoRoT-2b was also measured with Spitzer (Gillon et al., 2010), and in H and K bands (Alonso et al., 2010). In Figure 4.23, these values are compared to the secondary eclipse depths in the CoRoT bandpass.

In the near future, it will be interesting to compare these measurements of secondary eclipses for CoRoT-1b and CoRoT-2b with planet atmosphere models (e.g. Barman et al. 2005) and with black bodies, to see how the models compare to the observations.

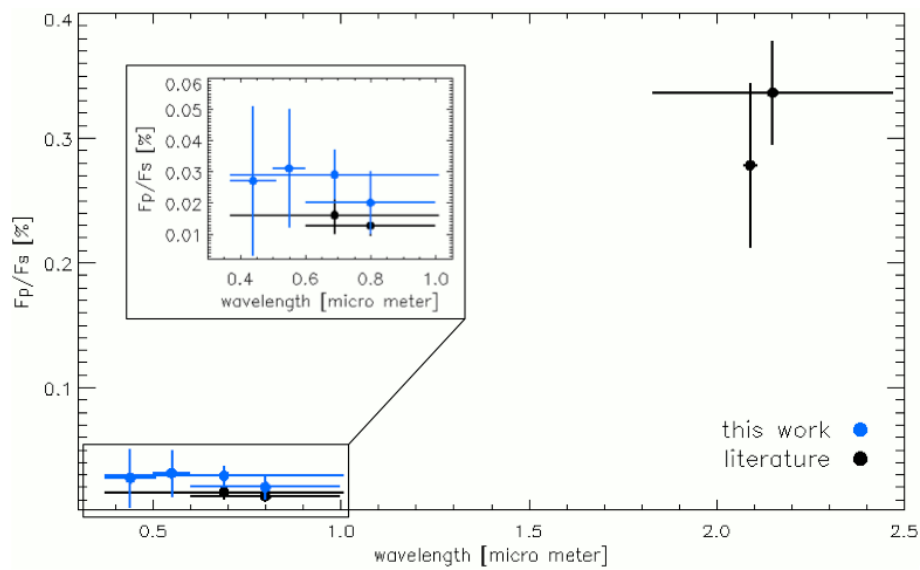


Figure 4.22: The depth of the secondary eclipse of CoRoT-1b is plotted against the wavelength of the observations.

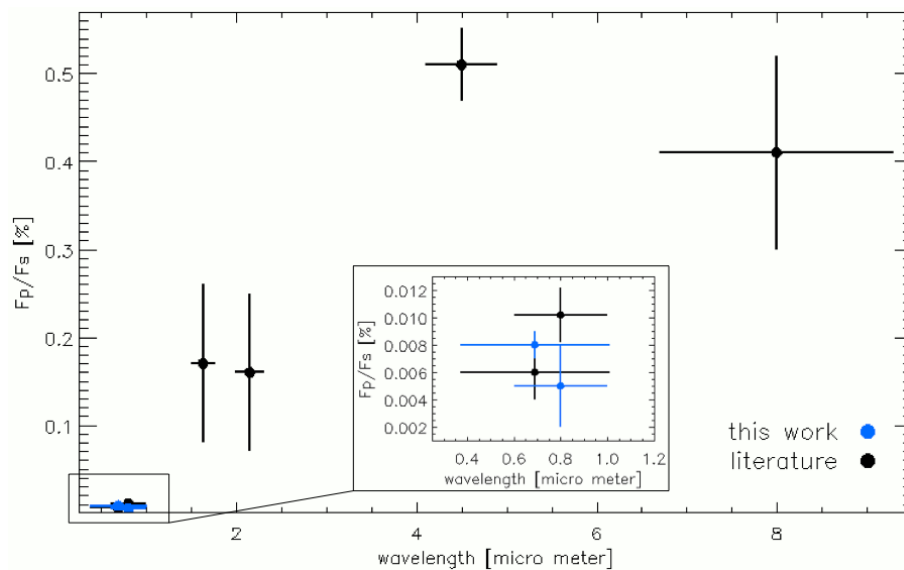


Figure 4.23: The depth of the secondary eclipse of CoRoT-2b is plotted against the wavelength of the observations.

4.4.2 Performance of the IRF

The IRF filters the stellar variability down to a level that allows us to detect, in their phase-folded light curve, the secondary eclipse of close-in large planets (e.g. CoRoT-1b and CoRoT-2b) and the planet orbital phase variation in some cases (e.g. CoRoT-1b).

In order to keep the noise level low in the phase-folded light curve, it helps to:

- chose the appropriate IRF-filtering parameters (timescale and binsize), small enough to filter as much variability as possible but large enough not to change the noise

propriety (Section 4.2.4).

- cut out all the orbits containing a jump in flux, before filtering
- select an integer number of planetary orbits
- select an integer number of the stellar rotation period (in the case of active stars)
- evaluate (over the whole light curve or over re-combined individual chunks) and remove flux modulations at orbital period of the CoRoT satellite, post filtering
- remove planet orbits with residual discontinuities in the filtered light curve, post filtering
- keep as many planetary orbits as possible to increase the signal to noise ratio
- clip 3σ outliers, post filtering

4.4.3 Limitations

In the case of CoRoT-1b, the main limitation is the level of photon noise which can only be improved by observing more planet orbits and/or by using a larger space telescope. In the case of CoRoT-2b, the main limitation is the residual stellar variability at the planetary orbital phase (localise or spread over the phase-folded light curve).

A 2σ difference between the secondary eclipse depth for CoRoT-1b published in Alonso et al. (2009b) and that found here highlights the fact that secondary eclipse depths derived from optical light curves at the limit of significance are still strongly dependent on the details of the light curve preprocessing.

Even after careful filtering (as described above), some significant correlated noise features can remain in the phase-folded light curve (e.g. CoRoT-2) and can create false detection or reduce the detection significance of a real secondary eclipse. These correlated noise features can come from:

- the original light curve, as a large feature in a single planet orbit can still be apparent in the phase-folded light curve, even after averaging with non affected orbits. One can attempt to remove these correlated features by improving the filtering of the signal outside that of the planetary orbital period (smaller *timescale* and *binsize*), and/or by cutting out before the filtering the planetary orbits where these correlated features occur.
- the filtering process (see Section 4.2.4), in which case re-doing the IRF-filtering with a smaller *timescale* and/or a larger *binsize* might smooth out these features. Smaller *timescale* will identify these features as stellar variability and they will not be passed into the transit signal. If the features are too sharp, smaller *timescale* will not be enough, and some residual features will end up in the transit signal.

These features will be binned with the non-affected orbits, and will contaminate them. In this case, a larger `binsize` will sum over features with more non-affected points, smoothing out the irregularity. Nevertheless, using a small `timescale` and large `binsize` is a trade off between filtering out the maximum of stellar variability signal and still preserving the transit signal intact.

Both these options were tried in the case of CoRoT-2b, but still leave stellar variability residuals at the planet orbital period larger than the amplitude of the secondary eclipse.

Once the secondary eclipse of a planet is detected and its depth measured, the next step is to extract the albedo and the equilibrium temperature of the planet from this measurement.

When observing in the infrared, the dominating flux of the planet is its thermal emission. Assuming the planet is in thermal equilibrium, the planet equilibrium temperature can be derived from the planet's brightness temperature. This gives access to a series of combinations of albedo and redistribution factors compatible with the planet.

When observing at shorter wavelengths (blue and shorter), the dominating flux of the planet is reflected light (for large value of the albedo, value depending on the size of the planet and the distance to its star) and the albedo can be measured. The orbital phase variation in thermal emission can give a clue about the redistribution factor. If the redistribution is small, the point of maximum flux in the phase curve will correspond to the phase of the secondary eclipse, and the larger the distribution factor the larger the difference in phase between the maximum in flux of the phase variation and the secondary eclipse. When these three measurements can be obtained, the possible combinations of albedos and redistribution factors compatible with the planet can be narrowed down.

When integrating the planetary flux over the visible, such as in the CoRoT light curve, the thermal emission and the reflected light are both present. With the CoRoT light curve, we have one measurement of the depth of the secondary eclipse and three unknowns: the albedo, the redistribution factor, and the fraction of thermal to reflected emission. If the depth of the secondary eclipse can be significantly measured in the CoRoT colour channel, an approximation of the fraction of thermal to reflected light can be derived. Unfortunately, in practice the flux level in the red and green CoRoT channel are too small, even when combining two colour channels.

4.4.4 Future work

Other methods will need to be investigated to remove residual stellar variability at the planet orbital period, without affecting the planet orbital phase signal.

To extract a value for the albedo and the energy redistribution factor of a transiting planet, one would in general need a) a brighter star (low photon noise), b) a bright

planet (close-in and large giving a larger S/N) c) a rather quiet star (low residual stellar variability), d) a stable telescope and CCD camera (low correlated noise), and e) multi-wavelength observations of the secondary eclipse (e.g. ultra-violet, blue, green, red and infra-red, to separate the planet thermal emission from the reflected light).

In the near future, for planetary phase curves not affected by stellar variability, the orbital phase modelling will be modified to allow for non-sinusoidal periodic variations and maximum amplitude of the phase variation shifted from the phase of the secondary eclipse.

In addition, the method suggested in Section 4.2.3, to derive the uncertainty on this model will be implemented.

4.5 Conclusions

The performance of the IRF for the detection of planet secondary eclipses and orbital phases, was demonstrated. The parameters of the IRF were optimised for this task. The limits of the performance of the IRF are now better understood.

A convincing detection of the secondary eclipse of CoRoT-1b, and to some extent of its orbital variation, were achieved in the CoRoT white and red bandpasses. A less secure detection of the secondary eclipse of CoRoT-2b was also achieved in the CoRoT white bandpass.

Compared to the depths of the secondary eclipses at longer wavelengths, the depths in the CoRoT bandpass (optical) are smaller. This is expected as at longer wavelengths, planets are more luminous (thermal flux) compared to their star.